

# Removal of Phosphate by Adsorption with 2-Phenylimidazole-Modified Porous ZIF-8: Powder and Chitosan Spheres

Yu Zhao, Pei-Qing Yuan, Xin-Ru Xu, and Jingyi Yang\*

Cite This: *ACS Omega* 2023, 8, 28436–28447

Read Online

ACCESS |



Metrics &amp; More

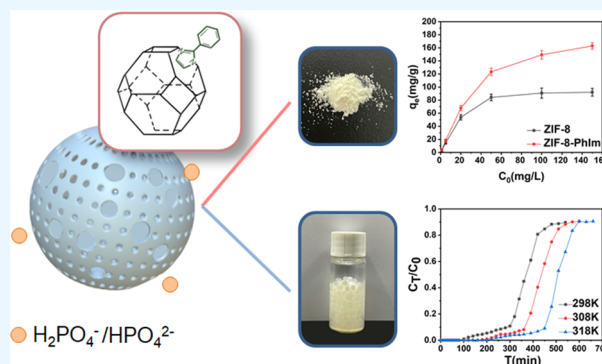


Article Recommendations



Supporting Information

**ABSTRACT:** Due to rapid socioeconomic development, increased phosphorus concentrations can cause eutrophication of water bodies, with devastating effects on environmental sustainability and aquatic ecosystems. In this study, ZIF-8-PhIm was prepared for phosphorus removal using 2-phenylimidazole via the solvent-assisted ligand exchange (SALE) method. The structure and composition of ZIF-8-PhIm were characterized by various methods, including X-ray diffraction (XRD), scanning electron microscopy (SEM), Fourier transform infrared spectroscopy (FT-IR),  $^1\text{H}$  nuclear magnetic resonance (NMR), X-ray photoelectron spectroscopy (XPS), and Brunauer–Emmett–Teller (BET) analysis. Compared to the ZIF-8 material, it exhibited a multistage pore structure with larger pore capacity and pore size, increased hydrophilicity, exposure of more adsorption sites, and also stronger electrostatic interaction. Under optimized conditions ( $T = 298\text{ K}$ ,  $C_0 = 150\text{ mg/L}$ , dose =  $0.2\text{ g/L}$ ), the adsorption capacity of ZIF-8-PhIm reached  $162.93\text{ mg/g}$ , which was greater than that of the ZIF-8 material ( $92.07\text{ mg/g}$ ). The Langmuir isotherm and pseudo-second-order kinetic models were suitable for describing the phosphate adsorption of ZIF-8-PhIm. The main effects of ZIF-8-PhIm on phosphate adsorption were Zn–O–P bonding and electrostatic interactions. It also had good regeneration properties. The ZIF-8-PhIm/CS spheres were prepared using chitosan (CS) as the cross-linking agent. The results of dynamic adsorption experiments on the spheres showed a saturation capacity of  $85.69\text{ mg/g}$  and a half-penetration time of  $514.15\text{ min}$  at  $318\text{ K}$  according to the fitted results.



## 1. INTRODUCTION

The increase in phosphorus concentrations in surface and groundwater systems due to excessive phosphorus discharges from human activities can cause eutrophication, which can lead to serious ecosystem damage (e.g., algal blooms), resulting in serious pollution and economic losses.<sup>1–3</sup> Currently, phosphorus removal usually relies on adsorption, chemical precipitation, and biodegradation.<sup>4–6</sup> Biological and chemical precipitation methods generate large amounts of sludge, which will increase the cost of post-treatment of solid waste.<sup>7</sup> In contrast, the adsorption method benefits from high phosphorus removal performance, simple operation, and low sludge production and has become the most prospective phosphorus removal and recovery technology.<sup>8–10</sup> Trinh et al. modified tea-activated carbon loaded with nanosilver and used to remove phosphate, reaching a maximum capacity of  $13.62\text{ mg/g}$ .<sup>11</sup> Han et al. used lignin as a raw material to produce magnetic bioactive carbon, and the maximum adsorption capacity was  $21.18\text{ mg/g}$ .<sup>12</sup> Natural adsorbents have a wide range of sources, but the adsorption capacity is low.

In recent years, zeolite-type imidazole skeletons (ZIF-8) have been considered to be highly prospective adsorbents owing to their large comparative surface area and the strong affinity of Zn ions for  $\text{PO}_4^{3-}$  ions.<sup>13</sup> Shams et al. used ZIF-8 for

phosphorus removal, which had an adsorption capacity of  $38.22\text{ mg/g}$ .<sup>14</sup> Bazzi et al. synthesized ZIF-8 under microwave and ultrasonic radiation and found that the microwave-synthesized ZIF-8 material had a high adsorption capacity of  $101.61\text{ mg/g}$ .<sup>15</sup> Huang et al. prepared a two-dimensional foliar ZIF (ZIF-L) adsorbent, having a maximum capacity of  $75.18\text{ mg/g}$ .<sup>13</sup>

The solvent-assisted ligand exchange (SALE) method is an indirect approach for the synthesis of alternative materials to replace or exchange organic linkers in the framework of MOFs, which can be used to improve certain properties.<sup>16–19</sup>

Kenyotha et al. used the SALE method to modify the synthesized ZIF-8 for  $\text{CO}_2$  adsorption, which has a higher pore volume and pore size with increased  $\text{CO}_2$  uptake.<sup>20</sup>

The main challenges in using MOFs as sorbents in practical applications are the difficulty of recovery in powder form and

Received: April 18, 2023

Accepted: July 14, 2023

Published: July 25, 2023



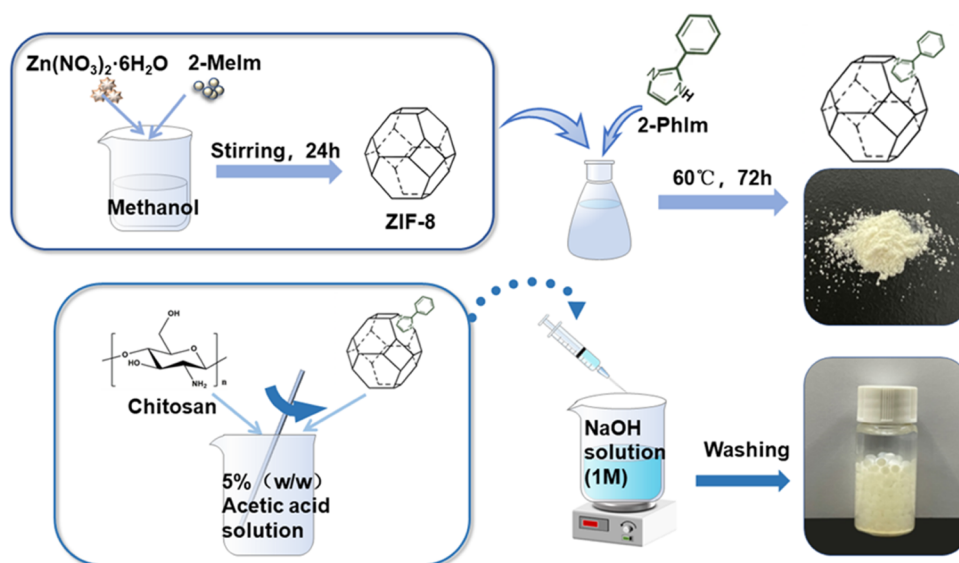


**Figure 1.** Illustration of the preparation of ZIF-8-PhIm (photograph courtesy of Yu Zhao. Copyright 2023).

the potential for secondary contamination.<sup>21–23</sup> Biosorbents from natural and biodegradable polymers have emerged as a hot topic in the area of adsorption. Chitosan has the advantages of being nontoxic and biodegradability. The combination of MOFs with chitosan (CS) is beneficial both for obtaining formed particle adsorbents and for increasing the adsorption capacity.<sup>24,25</sup>

Most MOF materials are microporous, which may prevent the larger tetrahedral phosphate anions from entering the cavities within the framework and affect the adsorption capacity.<sup>26</sup> ZIF-8-PhIm was synthesized for phosphate adsorption using the SALE method with ZIF-8 and 2-phenylimidazole (2-PhIm). ZIF-8-PhIm not only produced a multilevel pore structure with increased average pore volume and pore diameter but also exposed more active sites and had stronger electrostatic interaction. The structure of ZIF-8-PhIm was characterized by SEM, XRD, BET, <sup>1</sup>H NMR, XPS, and FT-IR methods. The phosphate adsorption effects of ZIF-8-PhIm and ZIF-8 were compared by the static adsorption method, and the regeneration performance and adsorption mechanism were discussed. ZIF-8-PhIm/CS sphere adsorbent was synthesized and subjected to dynamic adsorption.

## 2. MATERIALS AND METHODS

**2.1. Chemicals.** All reagents for analysis were processed without additional refinement. The detailed materials are presented in [Text S1](#).

**2.2. Synthesis of Adsorbent.** After the preparation of ZIF-8 by the solvent method, it was modified using the solvent-assisted ligand exchange method to obtain ZIF-8-PhIm, and ZIF-8-PhIm was combined with chitosan to obtain ZIF-8-PhIm/CS spheres. The detailed preparation method is shown in [Figure 1](#) and [Text S2](#).

**2.3. Characterization.** The structure of ZIF-8-PhIm and ZIF-8 was characterized by X-ray diffraction (XRD), scanning electron microscopy (SEM), <sup>1</sup>H NMR, BET, FT-IR, contact angle (CA), X-ray photoelectron spectroscopy (XPS) and  $\zeta$ -potential. The specific instruments and parameters are shown in [Text S3](#).

**2.4. Static Adsorption.** In the isothermal adsorption experiments, adsorbents at an addition level of 0.2 g/L were

added to 1–150 mg/L of the phosphate solution and adsorbed for 240 min. The procedure was as follows: 0.01 g of adsorbent was accurately weighed and added to a 100 mL conical flask, 50 mL of different concentrations of phosphate solution was added, sealed with a rubber stopper, and quickly transferred to a constant temperature shaker, the temperature of adsorption was controlled by the constant temperature shaker and the speed of the shaker was set at 170 rpm/min. After adsorption, the sample (3 mL) was passed through a 0.45  $\mu$ m filter membrane. The measurement of the phosphate solution concentration was carried out at 700 nm using the ammonium molybdate spectrophotometric method (Chinese standard GB11893-89) with an ultraviolet–visible spectrophotometer (Shunyu Hengping Scientific Instruments Co., Ltd., UV-1000).

The adsorption capacity was measured using [eq 1](#)

$$q_t = \frac{(C_0 - C_t) \cdot V}{m} \quad (1)$$

where  $q_t$  is the adsorption capacity for phosphate at moment  $t$ , mg/g;  $m$  is the mass of the adsorbent, g;  $V$  is the volume of the solution, L;  $C_0$  is the concentration of the initial phosphate solution, mg/L; and  $C_t$  is the concentration of phosphate left in solution at time  $t$ , mg/L.

**2.5. Dynamic Adsorption.** The column for the dynamic adsorption experiments was a custom-made glass adsorption column with an insulated jacket, 300 mm high and 8 mm inner diameter. The adsorbent was filled to a height of 200 mm and the remaining space was filled with glass packing. The experimental temperature was controlled by circulating water. The phosphate solution was flowed through the adsorption column in a top-down manner, using a dual-column micro-pump to control the flow rate to 1 mL/min. The adsorbed solution was gathered at regular intervals at the lower end of the column and the absorbance of the collected solution was measured.

**2.6. Regeneration Methods.** 20 mg of the adsorbed sample was washed with 100 mL of NaOH solution (0.01 mol/L). The sample was whipped at 600 rpm for 8 h, filtered and washed to neutral, and then desiccated in an oven at 120 °C for 12 h. Then, the next cycle was carried out in a 50 mg/L phosphate solution.

### 3. RESULTS AND DISCUSSION

**3.1. Characterization of ZIF-8-PhIm and ZIF-8.** Figure 2 displays the XRD images of ZIF-8-PhIm and ZIF-8. ZIF-8-

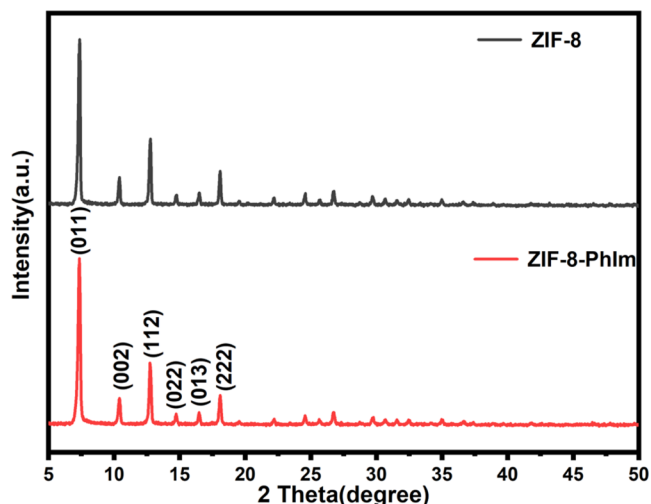


Figure 2. XRD images of ZIF-8-PhIm and ZIF-8.<sup>27</sup>

PhIm has the same characteristic peaks of ZIF-8.<sup>27</sup> The spectra of ZIF-8-PhIm and ZIF-8 were essentially identical at 7.3° (011), 10.4° (002), 12.7° (112), 14.7° (022), 16.4° (013), and 18.0° (222), indicating that the backbone of ZIF-8 was preserved after the substitution of 2-methylimidazole with 2-phenylimidazole.<sup>28</sup>

Figure 3 shows the SEM graphics of ZIF-8-PhIm and ZIF-8. After an exchange with 2-phenylimidazole, the particle size of ZIF-8-PhIm became larger, with the average grain size of ZIF-8 being  $\sim 185.55$  nm, while ZIF-8-PhIm had an average grain size of 241.74 nm.

From the analysis of the <sup>1</sup>H NMR spectrum of ZIF-8-PhIm, it can be obtained that 2-methylimidazole was partially substituted by 2-phenylimidazole in ZIF-8 (Figure 4).<sup>27</sup> For ZIF-8-PhIm, the signal of the CH=CH proton in 2-methylimidazole was observed at 7.19 ppm. The key signals for the neighbor substitution proton (2',6') and the imidazole aromatic proton (4,5) of 2-phenylimidazole were observed at 7.73 and 7.38 ppm, confirming the substitution of 2-methylimidazole by 2-phenylimidazole during SALE. The exchange ratio is  $\sim 1:0.04$  depending upon the integral proportion of the CH=CH proton of 2-methylimidazole (7.19 ppm, 2H) to the ortho-substituted proton of 2-phenylimidazole (7.73 ppm, 2H).<sup>20</sup> The relatively low exchange rate due to the spatial site resistance effect of the larger volume of the benzene ring allows the exchange of the ligand with the imidazole derivative to occur mainly on the surface of the nanoparticles.<sup>29</sup>

The N<sub>2</sub> sorption–desorption isotherm curves and pore size distributions of ZIF-8-PhIm and ZIF-8 are illustrated in Figure Sa,b. As can be observed from Figure Sa, the N<sub>2</sub> sorption–desorption isotherm curves conformed to a typical type I isotherm, suggesting that the pores were primarily microporous in structure.<sup>30</sup> The pore structure parameters and specific surface area are presented in Table 1.

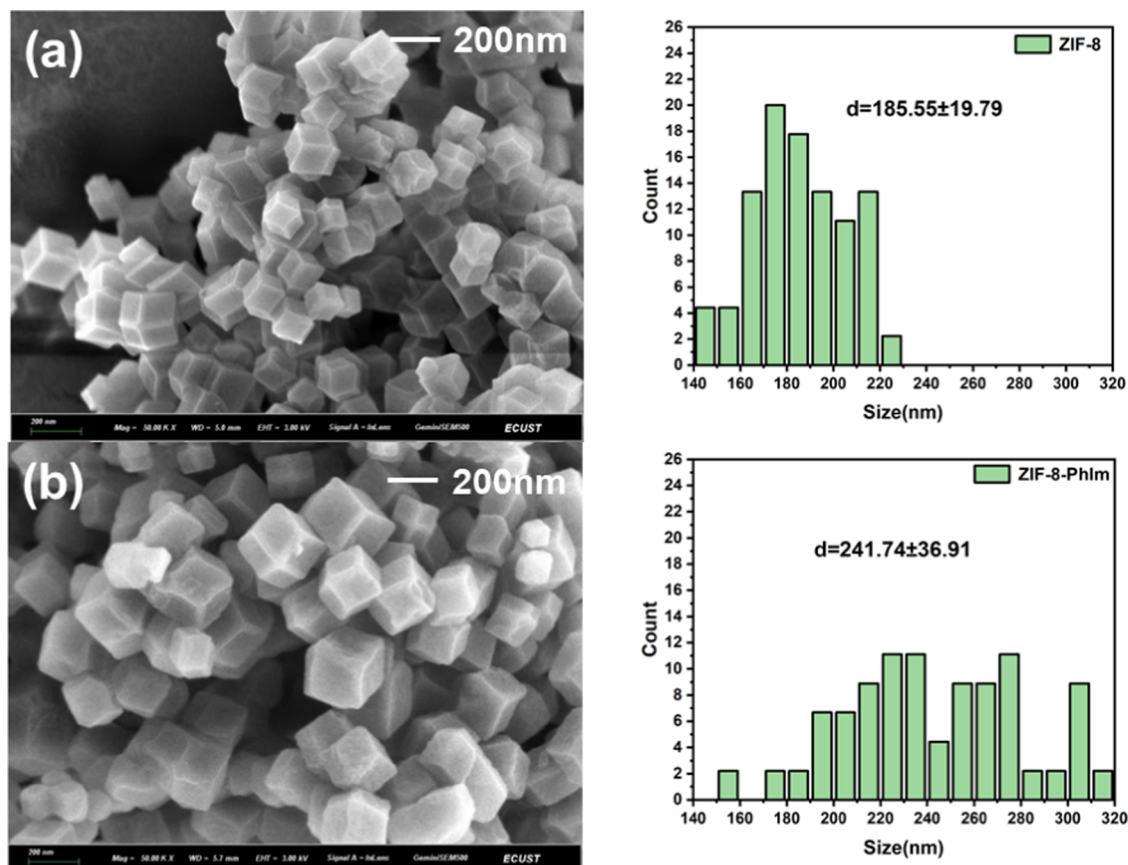


Figure 3. SEM images and particle size distributions of (a) ZIF-8 and (b) ZIF-8-PhIm.

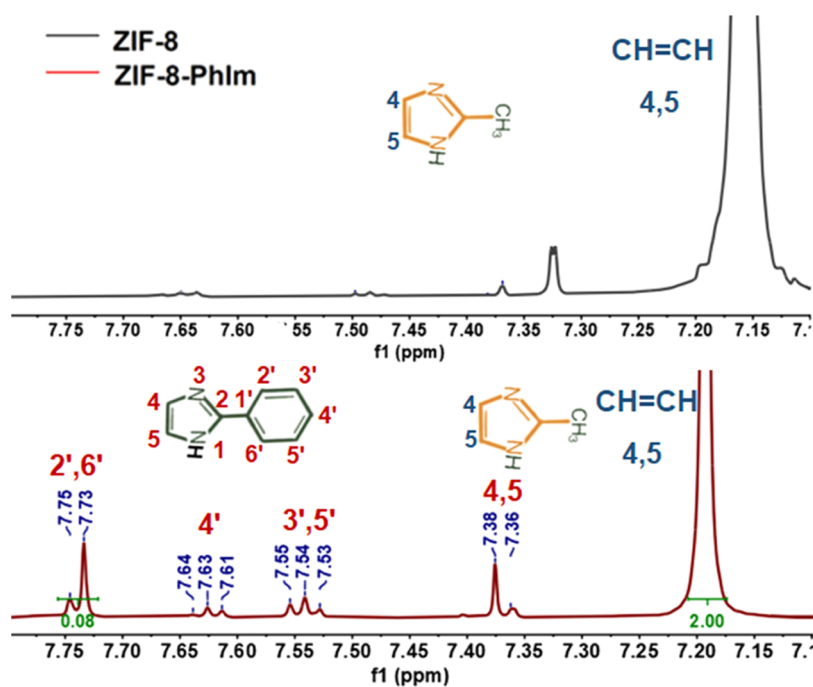


Figure 4.  $^1\text{H}$  NMR spectra of ZIF-8-PhIm and ZIF-8.<sup>27</sup>

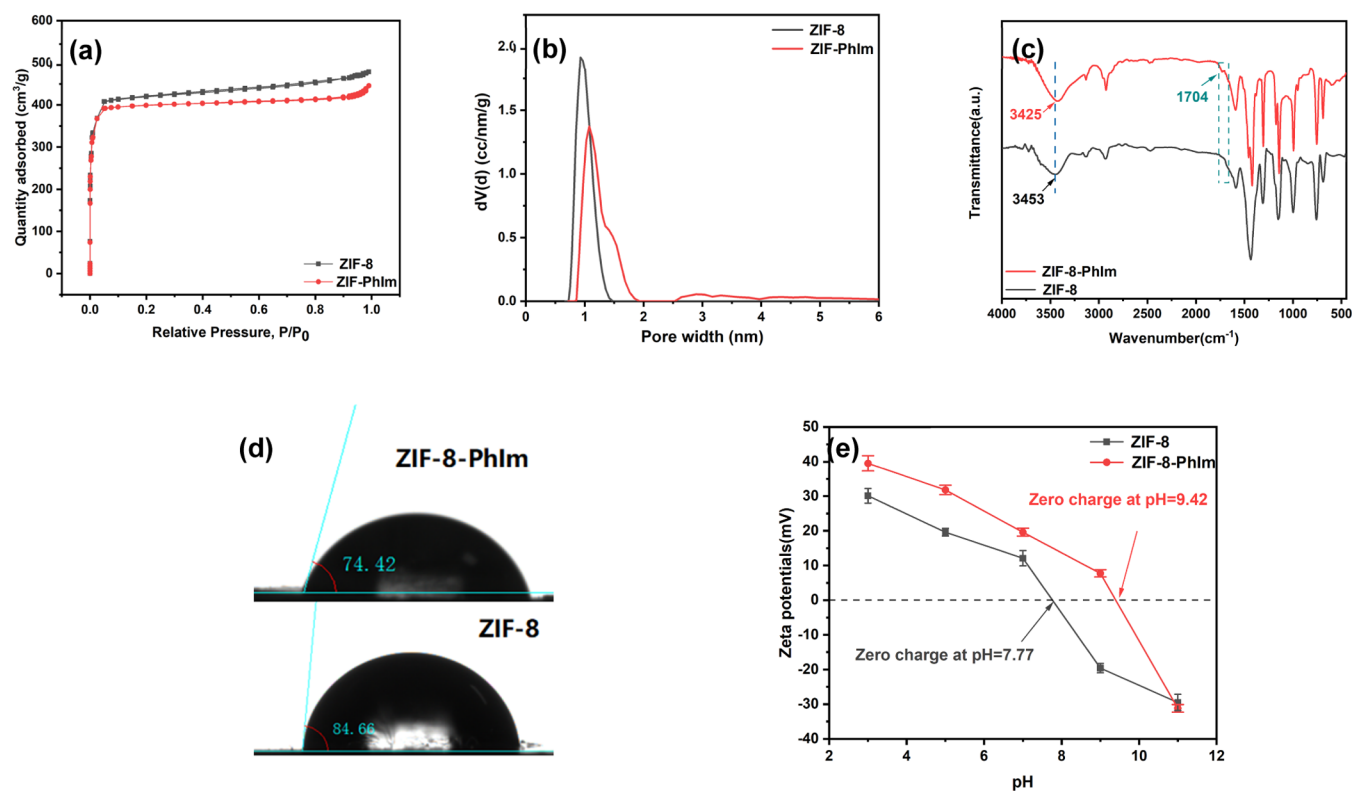
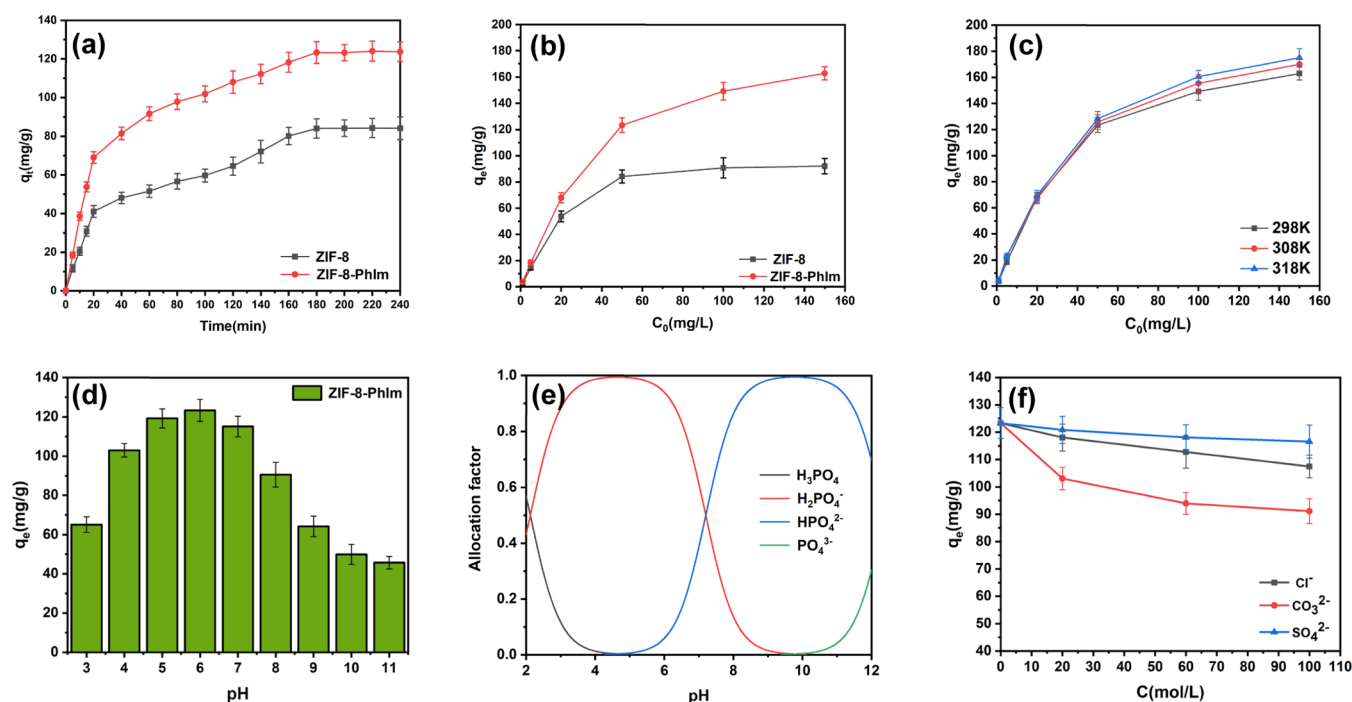


Figure 5. (a)  $\text{N}_2$  adsorption and desorption isotherms of ZIF-8-PhIm and ZIF-8, (b) pore size distribution of ZIF-8-PhIm and ZIF-8, (c) FT-IR images of ZIF-8-PhIm and ZIF-8,<sup>27</sup> and (e)  $\zeta$ -potential of ZIF-8-PhIm and ZIF-8.

Table 1. Parameters of the Pore Structure

sample	surface area ( $\text{m}^2/\text{g}$ )	average pore diameter (nm)	pore volume ( $\text{cm}^3/\text{g}$ )	micropore volume ( $\text{cm}^3/\text{g}$ )	mesopore volume ( $\text{cm}^3/\text{g}$ )	mesopore volume percentage (%)
ZIF-8-PhIm	1663.79	2.08	0.85	0.54	0.31	36.47
ZIF-8	1700.39	1.85	0.79	0.60	0.19	24.05



**Figure 6.** (a) Effect of time on phosphate adsorption ( $T = 298$  K; dose = 0.2 g/L;  $C_0 = 50$  mg/L), (b) effect of initial concentration on phosphate adsorption ( $T = 298$  K; dose = 0.2 g/L;  $t = 240$  min), (c) effect of temperature on phosphate adsorption (dose = 0.2 g/L;  $t = 240$  min), (d) effect of pH on phosphate adsorption ( $T = 298$  K;  $C_0 = 50$  mg/L; dose = 0.2 g/L;  $t = 240$  min), (e) phosphate ion morphology at different pH values, and (f) effects of ion concentration on phosphate adsorption ( $T = 298$  K; dose = 0.2 g/L;  $C_0 = 50$  mg/L;  $t = 240$  min).

Although the specific surface area of ZIF-8-PhIm ( $1663.79$   $\text{m}^2/\text{g}$ ) decreased compared to ZIF-8 ( $1700.39$   $\text{m}^2/\text{g}$ ), its pore diameter and pore volume ( $2.08$  nm,  $0.85$   $\text{cm}^3/\text{g}$ ) increased compared to ZIF-8 ( $1.85$  nm,  $0.79$   $\text{cm}^3/\text{g}$ ), and the proportion of mesopores increased from  $24.05$  to  $36.47\%$ . This is related to the larger volume of 2-phenylimidazole during the exchange process. Thus, ZIF-8-PhIm exposes more active sites than ZIF-8 and is more favorable for the adsorption of the target contaminant.

In the FT-IR spectra (Figure 5c), a characteristic peak was observed at  $1704$   $\text{cm}^{-1}$ , belonging to the octave and group frequency bending vibrations on the benzene ring  $\delta_{\text{CH}}$ . The weak intensity of the characteristic peak is due to the low exchange ratio of imidazole. For the  $-\text{OH}$  absorption peak, the wavenumber changes from  $3453$   $\text{cm}^{-1}$  (original ZIF-8) to  $3425$   $\text{cm}^{-1}$  (ZIF-8-PhIm), with a noticeable shift toward lower wavenumbers and an increase in hydrogen bonding.

The droplet image (Figure 5d) shows that, unlike ZIF-8 ( $84.66^\circ$ ), the contact angle of ZIF-8-PhIm is reduced by about  $10^\circ$  to  $74.42^\circ$ .<sup>27</sup> This is due to the enhanced hydrogen bonding, which makes it easier for molecules to bind to water molecules, thus enhancing hydrophilicity. The hydrophilic nature of the ZIF-8-PhIm material facilitates the exposure of adsorption sites.<sup>13</sup>

The  $\zeta$ -potentials are shown in Figure 5e. The  $\zeta$ -potential of ZIF-8-PhIm reduced gradually with the increase of pH. The isoelectric point of ZIF-8-PhIm appeared later than that of ZIF-8. The conjugation of benzene and imidazole rings in 2-PhIm leads to a decrease in the density of the electron cloud on the imidazole ring, which results in an enhanced positivity of Zn. The more positive charges on the surface of ZIF-8-PhIm, the more anions are attracted through electrostatic interactions.

**3.2. Phosphate Adsorption by ZIF-8-PhIm.** **3.2.1. Effect of Time.** From Figure 6a, with the temperature of  $298$  K and the initial phosphate concentration of  $50$  mg/L, the adsorption speed was rapid for the two adsorbents in the first  $60$  min of contact time, then gradually decreased, and reached equilibrium after  $240$  min. This may be because of the large amount of active sites that were available on ZIF-8-PhIm in the early stages. With the increase of adsorption time, the binding sites became increasingly occupied by phosphate ions and the adsorption of phosphate slowed down.

**3.2.2. Effect of Initial Concentration and Temperature.** As can be seen in Figure 6b,c, as the initial phosphate concentration increases, the increase in adsorption amount was greater for ZIF-8-PhIm in comparison to ZIF-8. At  $T = 298$  K,  $C_0 = 150$  mg/L, and  $t = 240$  min, the maximum capacity for phosphate adsorption of ZIF-8-PhIm reached  $162.93 \pm 4.95$  mg/g, higher than that of ZIF-8 ( $92.07 \pm 5.90$  mg/g) and many previously published ZnO/ZIF-based adsorbents ( $54.82$ – $147.63$  mg/g, Table 2). As the temperature increased, the adsorption capacity changed little, but the adsorption rate of ZIF-8-PhIm increased, suggesting that the increase of temperature led to the increase of phosphate thermal movement.<sup>35</sup>

**3.2.3. Effect of pH.** pH affects both the charge properties of the form of phosphorus present in the solution and the adsorbent surface, which in turn affects the efficiency of phosphorus removal.<sup>36</sup> From Figure 6d, the adsorption capacity of ZIF-8-PhIm for phosphate was better under neutral conditions and weaker at pH values less than  $4$  and greater than  $7$ .

The ZIF material has an electrical charge on its surface, but whether or not it has a positive charge depends largely on the pH of the solution. From Figure 5e, the isoelectric point of ZIF-8-PhIm occurred at  $\text{pH} = 9.42$ . When the pH is below

**Table 2. Adsorption Capacity of Phosphate on Different Adsorbents**

material	adsorption capacity (mg/g)	reference
ZIF-8	54.82	13
2D ZIF-L	75.18	13
La@ZIF-8	147.63	31
HP-UiO-66(Zr)-OA	186.60	32
HP-UiO-66(Zr)-BA	80.20	32
Fe <sub>3</sub> O <sub>4</sub> @ZIF-67	116.59	33
diatomite composited with ZIF-8	13.46	34
ZnO@ZIF-8-US	101.61	15
ZnO@ZIF-8-MW	94.95	15
ZIF-8-PhIm	162.93 ± 4.95	this work

9.42, the surface of ZIF-8-PhIm was positively charged, favoring the adsorption of phosphate. Also, as shown in Figure 6e, pH has a large effect on the form of phosphorus present in the solution.<sup>37</sup> When the pH value is 3, a part of neutral H<sub>3</sub>PO<sub>4</sub> exists in the solution, and the adsorption capacity of the ZIF-8-PhIm material for neutral H<sub>3</sub>PO<sub>4</sub> is weak. As the solution pH increases, the concentration of H<sub>3</sub>PO<sub>4</sub> decreases sharply, the concentration of H<sub>2</sub>PO<sub>4</sub><sup>-</sup> increases, and the electrostatic effect is enhanced, so the adsorption capacity increases. Under weakly acidic conditions (pH = 4–7), H<sub>2</sub>PO<sub>4</sub><sup>-</sup> was the main species in solution, so the adsorption performance was well. When the pH was above 7, phosphate in solution was mainly in the form of HPO<sub>4</sub><sup>2-</sup>, which had a higher free energy of adsorption compared to that of H<sub>2</sub>PO<sub>4</sub><sup>-</sup> and was not conducive to adsorption by adsorbent materials through ligand exchange, resulting in a decline in the capacity of ZIF-8-PhIm as the pH of the solution increases.<sup>38,39</sup>

**3.2.4. Effect of Ion Concentration.** Chloride ions, sulfate ions, and carbonate ions were selected to examine the selectivity of ZIF-8-PhIm for phosphate adsorption. The obtained results are plotted in Figure 6f. The adsorption capacity dropped from 123.31 to 91.13 mg/g (carbonate ions), 107.45 mg/g (chloride ions), and 116.56 mg/g (sulfate ions) at a coexisting ion concentration of 100 mol/L. Of these, carbonate had a greater effect on adsorption, presumably because the addition of carbonate caused a significant change in the pH of the solution. When the concentration of carbonate ions was 100 mol/L, the pH of the solution was

8.59, so the adsorption capacity was affected by the pH value. It shows that certain ions may slightly affect phosphate adsorption, but the effect is not significant.

**3.3. Isotherms and Thermodynamics.** The Langmuir isotherm model and the Freundlich isotherm model were chosen for the fitting of the data.<sup>40</sup> According to the results of the model fit (Figure 7a,b and Table 3), the Langmuir

**Table 3. Parameters of the Isotherm Models for Phosphate Adsorption on ZIF-8-PhIm**

models	298 K	308 K	318 K	
Langmuir	$q_m$ (mg/g)	174.68	183.27	187.16
	$K_L$ (L/mg)	0.09	0.08	0.09
	$R^2$	0.998	0.986	0.987
Freundlich	$1/n$	0.35	0.33	0.33
	$K_F$ (mg <sup>1-n</sup> g <sup>-1</sup> L <sup>-n</sup> )	31.98	36.33	37.99
	$R^2$	0.932	0.960	0.961

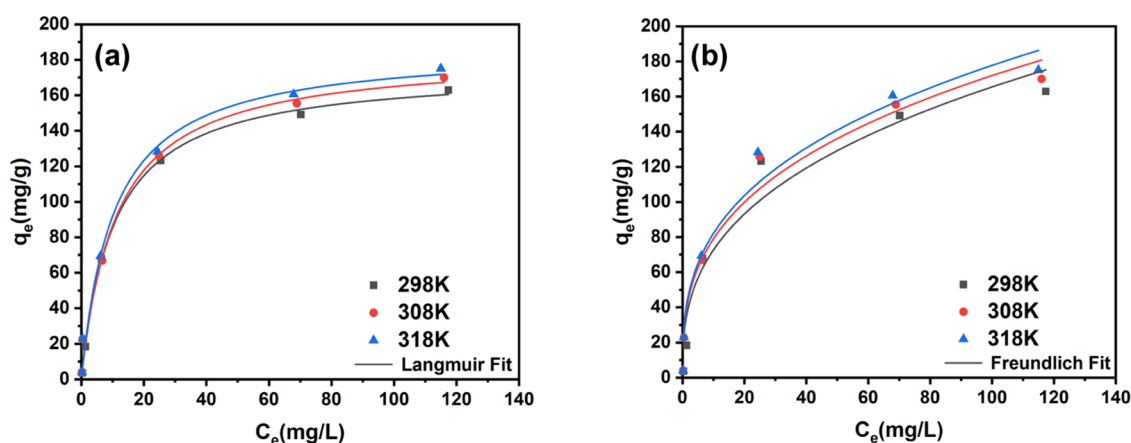
isotherm model ( $R^2 = 0.998$ ) provided a superior description of the phosphate adsorption behavior on ZIF-8-PhIm than the Freundlich isotherm model ( $R^2 = 0.932$ ). The Langmuir isotherm model indicated that phosphate adsorption by ZIF-8-PhIm was a spontaneous process in a single molecular layer with a relatively homogeneous spread of active centers. Based on the fit of the Langmuir isotherm model, the theoretical adsorption could reach 174.68 mg/g. Therefore, ZIF-8-PhIm is a useful material for phosphorus removal.

Further evaluation of the adsorption can be carried out by calculating thermodynamic parameters. The thermodynamic parameters are indicated in Table 4. The  $\Delta H$  is +32.65 kJ/mol

**Table 4. Thermodynamic Parameters of Phosphate Adsorption by ZIF-8-PhIm**

T (K)	$\Delta G$ (kJ/mol)	$\Delta H$ (kJ/mol)	$\Delta S$ (J/(K·mol))
298.15	-3.95	32.65	122.81
318.15	-6.40		

and the adsorption process is a process of heat absorption. The  $\Delta H$  is higher than 29 kJ/mol, indicating the presence of chemisorption.<sup>41</sup>  $\Delta G < 0$ , which suggests that the adsorption process occurs spontaneously.  $\Delta S > 0$ , which suggests that phosphate adsorption is a process of increasing entropy.

**Figure 7.** (a) Isotherm curves of phosphate adsorption fitting with the Langmuir model and (b) the isotherm curves of phosphate adsorption fitting with the Freundlich model.

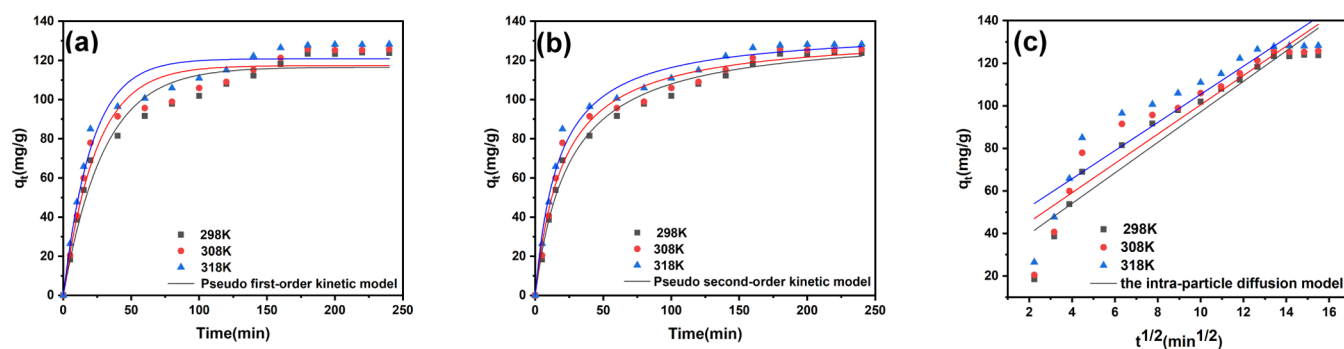


Figure 8. (a) Kinetic curves of the adsorption fitting with the pseudo-first-order kinetic model, (b) kinetic curves of the adsorption fitting with the pseudo-second-order kinetic model, and (c) kinetic curves of phosphate adsorption fitting with the intraparticle diffusion kinetic model.

Table 5. Parameters of the Kinetic Adsorption Models for Phosphate Adsorption on ZIF-8-PhIm

models		298 K	308 K	318 K
pseudo-first-order kinetic model	$k_1$ ( $\text{min}^{-1}$ )	0.037	0.041	0.048
	$q_{e1, \text{cal}}$ (mg/g)	112.34	117.32	120.64
	$q_{e1, \text{exp}}$ (mg/g)	123.31	125.73	128.27
	$R^2$	0.964	0.956	0.961
pseudo-second-order kinetic model	$k_2$ ( $\text{g}/(\text{mg}\cdot\text{min})$ )	$3.109 \times 10^{-4}$	$3.669 \times 10^{-4}$	$4.358 \times 10^{-4}$
	$q_{e2, \text{cal}}$ (mg/g)	133.01	134.04	135.76
	$q_{e2, \text{exp}}$ (mg/g)	123.31	125.73	128.27
	$R^2$	0.987	0.983	0.986
the intraparticle diffusion model	$k_{\text{ip}}$ ( $\text{mg g}^{-1} \text{min}^{1/2}$ )	7.16	6.88	6.61
	C	25.43	31.59	39.25
	$R^2$	0.899	0.871	0.853

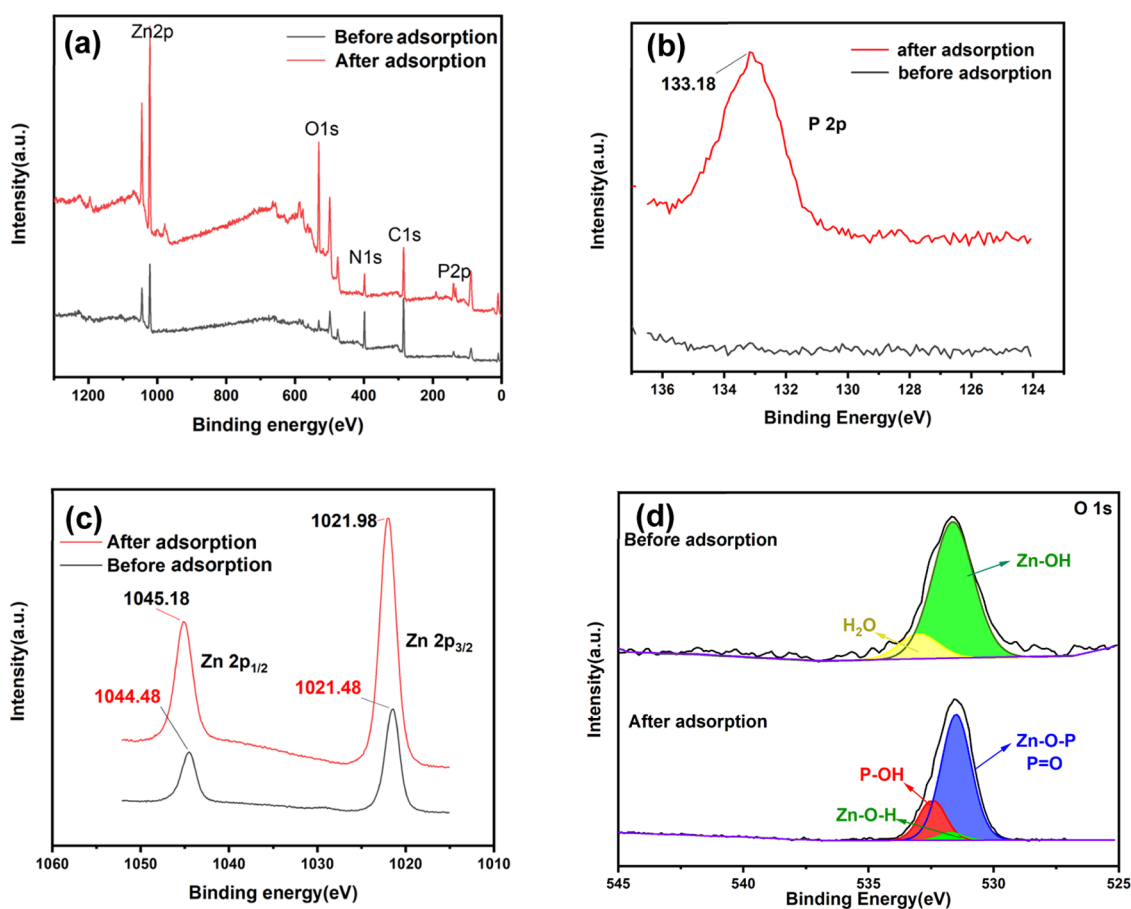


Figure 9. XPS of ZIF-8-PhIm before and after adsorption: (a) full score, (b) P 2p, (c) Zn 2p, and (d) O 1s.

**3.4. Adsorption Kinetics.** Pseudo-first-order, pseudo-second-order, and VM model were adopted to fit ZIF-8 and ZIF-8-PhIm adsorption kinetic curves.<sup>42–44</sup>

The fitting results from Figure 8 and Table 5 show that the pseudo-second-order kinetic model ( $R^2 = 0.987$ ) fitted better in comparison to the pseudo-first-order kinetic model ( $R^2 = 0.964$ ). The adsorption kinetics were not consistent with the VM model and the pseudo-first-order model. In the intraparticle diffusion kinetic model, if the fitted curve passes through the origin and is governed by good linearity, then the adsorption is dominated by the intraparticle spreading process. Nevertheless, if the fitted curve does not go through the origin, the rate-control step is the film spreading process. As illustrated in Figure 8c, the lines did not go through the origin, which suggested that the process was dominated by the film spreading mechanism.<sup>45</sup> Therefore, the pseudo-second-order kinetic model was more suited to characterize the adsorption process, indicating the presence of chemisorption.

Because the results of the pseudo-second-order kinetic model fit were closest to the experimental data, the parameters fitted by the pseudo-second-order kinetic model were employed to obtain the activation energy. The activation energy for the ZIF-8-PhIm adsorption process was 13.29 kJ/mol, lower than 20–30 kJ/mol, which indicated the presence of physical adsorption.<sup>46</sup>

**3.5. Adsorption Mechanism.** In the XPS spectrum of P 2p (Figure 9b), the newly generated peak at 133.18 eV confirmed the adsorption of phosphate. However, this P 2p peak was moved 0.52 eV to the lower energy side in comparison to the pure  $\text{KH}_2\text{PO}_4$  (133.7 eV), indicating the strong chemical bonding of phosphate on ZIF-8-PhIm.<sup>13,47</sup>

Prior to adsorption, the XPS spectrum of Zn 2p showed two peaks (Figure 9c), which can be classified as Zn 2p<sub>3/2</sub> and Zn 2p<sub>1/2</sub> orbitals (1021.48, 1044.48 eV), respectively. After adsorption, the Zn 2p<sub>3/2</sub> peak moved 0.5 eV and the Zn 2p<sub>1/2</sub> peak moved 0.7 eV toward the high energy side, revealing a strong interaction between  $\text{Zn}^{2+}$  and  $\text{PO}_4^{3-}$ .

The deconvolution of the O 1s spectrum gave three peaks: Zn–O–P/P=O at 531.50 eV, Zn–OH (hydroxyl group combined with Zn) at 531.71 eV, and P–OH (hydroxyl in  $\text{HPO}_4^{2-}/\text{H}_2\text{PO}_4^-$ ) at 532.40 eV (Figure 9d, Table 6).<sup>48–50</sup>

**Table 6. Binding Energies and Relative Contents in the O 1s Profiles of ZIF-8-PhIm Before and After Adsorption**

species	before adsorption		after adsorption	
	binding energy (eV)	atom %	binding energy (eV)	atom %
O 1s	Zn–O–P	531.50	531.50	76.35
	Zn–OH	531.71	531.71	3.62
	H <sub>2</sub> O	533	533	
	P–OH	532.40	532.40	20.03

The peak of Zn–OH decreased significantly following the production of the Zn–O–P peak compared to before adsorption, indicating that the Zn–OH group on the surface can dehydrate with P–OH in the phosphate to produce a stronger Zn–O–P bond. This indicates that hydroxyl groups are critical in the process of phosphate adsorption through strong complexation.

The infrared spectra of ZIF-8-PhIm were characterized. Figure 10 displays the FT-IR profile of the original and loaded adsorbent. The functional groups remained basically un-

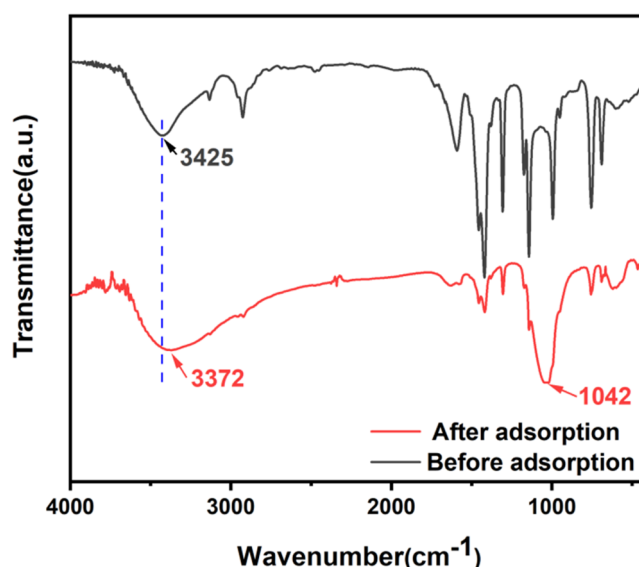


**Figure 10.** FT-IR spectrum of ZIF-8-PhIm before and after phosphate adsorption.

changed before and after adsorption, which indicated that the structure of the material was not destroyed. The characteristic peak at 1042  $\text{cm}^{-1}$ , representing the asymmetric stretching vibration of P–O, suggests that the phosphate was successfully adsorbed. For the –OH absorption peak, the wavenumber varied from 3425 to 3375  $\text{cm}^{-1}$  after adsorption, significantly shifting toward the lower wavenumbers, indicating enhanced hydrogen bonding. It is indicated that the phosphate exchanged ligands with the –OH group on ZIF-8-PhIm.<sup>51</sup>

In summary, the mechanism of phosphate adsorption can be summarized in two key interactions: (1) Zn–O–P bonding and (2) electrostatic attraction of the negative phosphate ion to the positive ZIF-8-PhIm surface. The increase in pore size and pore capacity of ZIF-8-PhIm increased hydrophilicity and exposed more active sites for adsorption (Figure 11).

**3.6. Regeneration Experiment.** It could be seen from the XRD pattern (Figure 12a) that the crystalline shape did not change after regeneration by a 0.01 mol/L NaOH ethanol solution. Compared to the fresh adsorbent, the amount of phosphate adsorbed by the regenerated ZIF-8-PhIm decreased from  $123.31 \pm 5.64$  mg/g initially to  $101.81 \pm 4.16$  mg/g after five regeneration treatments (Figure 12b). This decline may be due to damage to ZIF-8-PhIm by the alkali regeneration solution; on the other hand, the regeneration of the minority chemical bonds between ZIF-8-PhIm and the phosphate may be incomplete. As a result, ZIF-8-PhIm has good reusability.

**3.7. Dynamic Adsorption.** **3.7.1. Effect of Temperature.** The performance of ZIF-8-PhIm/CS for phosphate adsorption was investigated at temperatures of 298, 308, 318 K (Figure 13). From the penetration curve, the saturation adsorption capacity was obtained by integrating the curve and calculated as shown in eq 2

$$q = \frac{v}{1000m} \int_0^t (C_0 - C_t) dt \quad (2)$$

where  $q$  is the adsorption capacity of ZIF-8-PhIm/CS, mg/g;  $m$  is the adsorbent weight, g;  $v$  is the phosphate solution flow rate, mL/min;  $t$  is the adsorption time, min;  $C_0$  is the phosphate concentration of input port, mg/L;  $C_t$  is the phosphate concentration of output port at time  $t$ , mg/L.

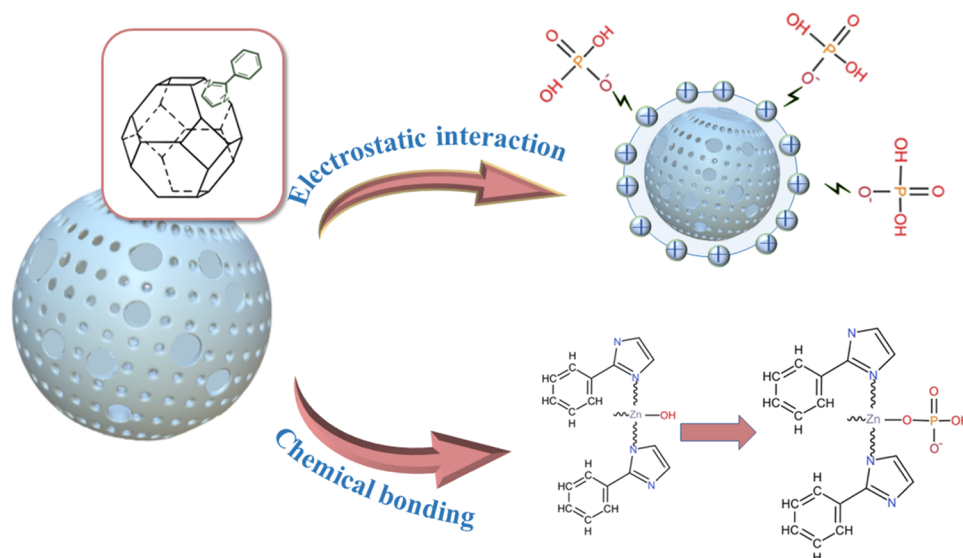


Figure 11. Mechanism of phosphate adsorption by ZIF-8-PhIm.

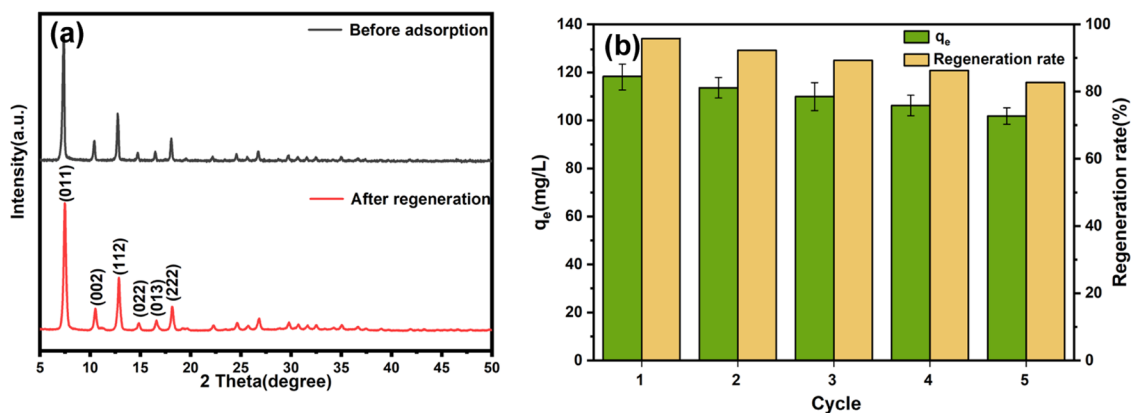


Figure 12. (a) XRD of ZIF-8-PhIm before adsorption and after regeneration and (b) the adsorption capacity of phosphate and regeneration efficiency of ZIF-8-PhIm after adsorption–desorption cycles ( $T = 298$  K; dose = 0.2 g/L;  $C_0 = 50$  mg/L;  $t = 240$  min).

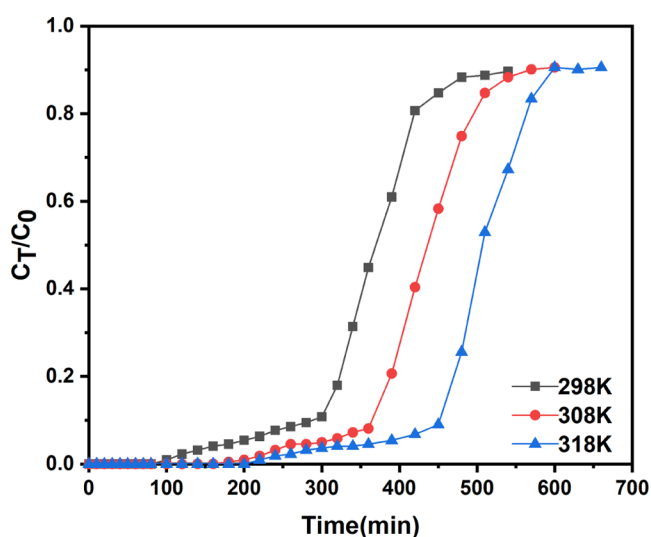


Figure 13. Breakthrough curves at different temperatures.

The adsorption capacity of chitosan spheres was relatively low at 1.78 mg/g at 298 K (Figure S1). The phosphate adsorption capacities of ZIF-8-PhIm/CS spheres were 63.10,

73.41, and 85.69 mg/g, respectively, at different temperatures (298, 308, 318 K). With temperature increasing, the phosphate adsorption capacity of ZIF-8-PhIm/CS spheres increased.

**3.7.2. Column Adsorption Model.** Thomas model and Yoon–Nelson model were chosen to carry out the fitting of the breakthrough curves. The fitted results and model parameters are given in Figure 14 and Table 7. The dynamic equilibrium adsorption amounts predicted by the Thomas model at different temperatures were 62.29, 73.30, and 85.69 mg/g (298, 308, 318 K). The predicted results were similar to the experimental values. In addition, the half-penetration times for the Yoon–Nelson model fitted at different temperatures were 373.77, 439.80, and 514.15 min, respectively.

## 4. CONCLUSIONS

In this study, ZIF-8-PhIm was successfully prepared for phosphorus removal by the SALE method. The modification with 2-phenylimidazole resulted in ZIF-8-PhIm with a large pore size and improved hydrophilicity, which led to exposure of more active sites for adsorption. Under optimized conditions, the adsorption of phosphate by ZIF-8-PhIm reached 162.93 mg/g, which was greater than that of ZIF-8 (92.07 mg/g). The Langmuir isothermal adsorption model and the pseudo-second-order kinetic model can be used to

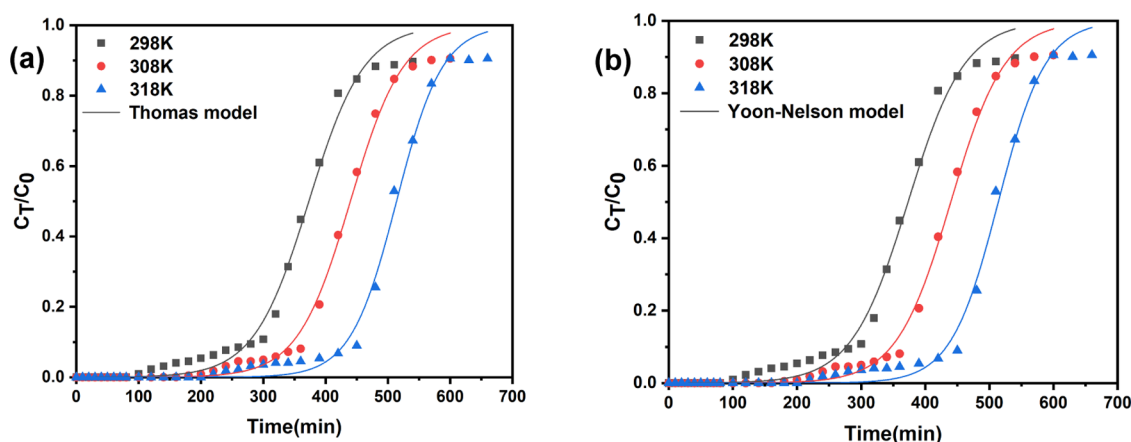


**Figure 14.** (a) Breakthrough curve of ZIF-8-PhIm/CS spheres fitting with the Thomas model and (b) the breakthrough curve of ZIF-8-PhIm/CS spheres fitting with the Yoon–Nelson model.

**Table 7. Parameters of the Thomas Model and Yoon–Nelson Model of Phosphate Adsorption on ZIF-8-PhIm/CS Spheres**

T (K)	Thomas				Yoon–Nelson		
	$K_{Tb}$ , mL/(min·mg)	$q_{model}$ , mg/g	$q_{exp}$ , mg/g	$R^2$	$K$ , min <sup>-1</sup>	$\tau$ , min	$R^2$
298	0.221	62.29	63.10	0.987	0.022	373.77	0.987
308	0.236	73.30	73.41	0.995	0.024	439.80	0.994
318	0.275	85.69	85.26	0.991	0.027	514.15	0.990

characterize the phosphate adsorption by ZIF-8-PhIm. The activation energy of adsorption ( $E_a$ ) was 13.29 kJ/mol. The mechanism of ZIF-8-PhIm for phosphate adsorption mainly involved Zn–O–P bonding and electrostatic attraction of phosphate ions to the surface of ZIF-8-PhIm. ZIF-8-PhIm also had excellent regeneration properties for phosphate. After five regeneration cycles, the adsorption capacity of ZIF-8-PhIm stabilized at 101.81 mg/g. ZIF-8-PhIm/CS hydrogel spheres were prepared using chitosan as the cross-linking agent. Dynamic adsorption experiments indicated that the Thomas model reached a capacity of 85.69 mg/g and the Yoon–Nelson model had a half-permeation time of 514.15 min at 318 K.

## ■ ASSOCIATED CONTENT

### Supporting Information

The Supporting Information is available free of charge at <https://pubs.acs.org/doi/10.1021/acsomega.3c02671>.

Chemicals used for experiments, synthesis procedure of adsorbent, characterization, model formulas, and breakthrough curve of CS spheres (PDF)

## ■ AUTHOR INFORMATION

### Corresponding Author

**Jingyi Yang** – International Joint Research Center of Green Energy Chemical Engineering, East China University of Science and Technology, Shanghai 200237, P. R. China; [orcid.org/0000-0002-4694-7860](https://orcid.org/0000-0002-4694-7860); Email: [jyyang@ecust.edu.cn](mailto:jyyang@ecust.edu.cn)

### Authors

**Yu Zhao** – International Joint Research Center of Green Energy Chemical Engineering, East China University of Science and Technology, Shanghai 200237, P. R. China; [orcid.org/0009-0000-9029-9007](https://orcid.org/0009-0000-9029-9007)

**Pei-Qing Yuan** – State Key Laboratory of Chemical Engineering, East China University of Science and

Technology, Shanghai 200237, P. R. China; [orcid.org/0000-0003-0797-963X](https://orcid.org/0000-0003-0797-963X)

**Xin-Ru Xu** – International Joint Research Center of Green Energy Chemical Engineering, East China University of Science and Technology, Shanghai 200237, P. R. China

Complete contact information is available at:

<https://pubs.acs.org/10.1021/acsomega.3c02671>

## Notes

The authors declare no competing financial interest.

## ■ ACKNOWLEDGMENTS

The authors are grateful to the National Natural Science Foundation of China (22178113).

## ■ REFERENCES

- (1) Wan, S.; Wang, S.; Li, Y.; Gao, B. Functionalizing biochar with Mg–Al and Mg–Fe layered double hydroxides for removal of phosphate from aqueous solutions. *J. Ind. Eng. Chem.* **2017**, *47*, 246–253.
- (2) Fang, L.; Wu, B.; Chan, J. K. M.; Lo, I. M. C. Lanthanum oxide nanorods for enhanced phosphate removal from sewage: A response surface methodology study. *Chemosphere* **2018**, *192*, 209–216.
- (3) Koh, K. Y.; Zhang, S.; Chen, J. P. Improvement of ultrafiltration for treatment of phosphorus-containing water by a lanthanum-modified aminated polyacrylonitrile membrane. *ACS Omega* **2020**, *5*, 7170–7181.
- (4) Singh, M.; Srivastava, R. K. Sequencing batch reactor technology for biological wastewater treatment: a review. *Asia-Pac. J. Chem. Eng.* **2011**, *6*, 3–13.
- (5) Bui, T. H.; Hong, S. P.; Yoon, J. Development of nanoscale zirconium molybdate embedded anion exchange resin for selective removal of phosphate. *Water Res.* **2018**, *134*, 22–31.
- (6) Zou, H.; Wang, Y. Phosphorus removal and recovery from domestic wastewater in a novel process of enhanced biological phosphorus removal coupled with crystallization. *Bioresour. Technol.* **2016**, *211*, 87–92.

- (7) Khalil, A. M. E.; Eljamal, O.; Amen, T. W. M.; Sugihara, Y.; Matsunaga, N. Optimized nano-scale zero-valent iron supported on treated activated carbon for enhanced nitrate and phosphate removal from water. *Chem. Eng. J.* **2017**, *309*, 349–365.
- (8) Yin, H.; Yan, X.; Gu, X. Evaluation of thermally-modified calcium-rich attapulgite as a low-cost substrate for rapid phosphorus removal in constructed wetlands. *Water Res.* **2017**, *115*, 329–338.
- (9) Tong, D.; Zhuang, J.; Lee, J.; Buchanan, J.; Chen, X. Concurrent transport and removal of nitrate, phosphate and pesticides in low-cost metal-and carbon-based materials. *Chemosphere* **2019**, *230*, 84–91.
- (10) Hu, L.; Chen, C.; Wang, X.; Hu, K.; Xu, Z.; Xu, W. ZIF-8 prepared in ionic liquid microemulsions for efficient capture of phosphate from water. *J. Chem. Sci.* **2022**, *134*, 62.
- (11) Trinh, V. T.; Nguyen, T. M. P.; Van, H. T.; Hoang, L. P.; Nguyen, T. V.; Ha, L. T.; Vu, X. H.; Pham, T. T.; Nguyen, T. N.; Quang, N. V.; Nguyen, X. C. Phosphate adsorption by silver nanoparticles-loaded activated carbon derived from tea residue. *Sci. Rep.* **2020**, *10*, No. 3634.
- (12) Han, T.; Lu, X.; Sun, Y.; Jiang, J.; Yang, W.; Jönsson, P. G. Magnetic bio-activated carbon production from lignin via a stream-lined process and its use in phosphate removal from aqueous solutions. *Sci. Total Environ.* **2020**, *708*, No. 135069.
- (13) Huang, C.; Zhang, H.; Zheng, K.; Zhang, Z.; Jiang, Q.; Li, J. Two-dimensional hydrophilic ZIF-L as a highly-selective adsorbent for rapid phosphate removal from wastewater. *Sci. Total Environ.* **2021**, *785*, No. 147382.
- (14) Shams, M.; Dehghani, M. H.; Nabizadeh, R.; Mesdaghinia, A.; Alimohammadi, M.; Najafpoor, A. A. Adsorption of phosphorus from aqueous solution by cubic zeolitic imidazolate framework-8: modeling, mechanical agitation versus sonication. *J. Mol. Liq.* **2016**, *224*, 151–157.
- (15) Bazzi, L.; Ayouch, I.; Tachallait, H.; Hankari, S. E. L. Ultrasound and microwave assisted synthesis of ZIF-8 from zinc oxide for the adsorption of phosphate. *Results Eng.* **2022**, *13*, No. 100378.
- (16) Stephenson, C. J.; Hupp, J. T.; Farha, O. K. Postassembly transformation of a catalytically active composite material, Pt@ ZIF-8, via solvent-assisted linker exchange. *Inorg. Chem.* **2016**, *55*, 1361–1363.
- (17) Pullen, S.; Fei, H.; Orthaber, A.; Cohen, S. M.; Ott, S. Enhanced photochemical hydrogen production by a molecular diiron catalyst incorporated into a metal-organic framework. *J. Am. Chem. Soc.* **2013**, *135*, 16997–17003.
- (18) Bury, W.; Fairen-Jimenez, D.; Lalonde, M. B.; Snurr, R. Q.; Farha, O. K.; Hupp, J. T. Control over catenation in pillared paddlewheel metal-organic framework materials via solvent-assisted linker exchange. *Chem. Mater.* **2013**, *25*, 739–744.
- (19) Abrahama, Y. W.; Tsai, C. W.; Niemantsverdriet, J. W. H.; Langner, E. G. Optimized CO<sub>2</sub> capture of the zeolitic imidazolate framework ZIF-8 modified by solvent-assisted ligand exchange. *ACS Omega* **2021**, *6*, 21850–21860.
- (20) Kenyotha, K.; Chanapatttharapol, K. C.; McCloskey, S.; Jantaharn, P. Water based synthesis of ZIF-8 assisted by hydrogen bond acceptors and enhancement of CO<sub>2</sub> uptake by solvent assisted ligand exchange. *Crystals* **2020**, *10*, 599.
- (21) Zhu, H.; Zhang, Q.; Zhu, S. Alginate hydrogel: a shapeable and versatile platform for in situ preparation of metal-organic framework-polymer composites. *ACS Appl. Mater. Interfaces* **2016**, *8*, 17395–17401.
- (22) Zhu, L.; Zong, L.; Wu, X.; Li, M.; Wang, H.; You, J.; Li, C. Shapeable fibrous aerogels of metal-organic-frameworks templated with nanocellulose for rapid and large-capacity adsorption. *ACS Nano* **2018**, *12*, 4462–4468.
- (23) Zhou, S.; Strømme, M.; Xu, C. Highly transparent, flexible, and mechanically strong nanopapers of cellulose nanofibers @metal-organic frameworks. *Chem. – Eur. J.* **2019**, *25*, 3515–3520.
- (24) Zhao, R.; Li, X.; Sun, B.; Zhang, Y.; Zhang, D.; Tang, Z.; Chen, X.; Wang, C. Electrospun chitosan/sericin composite nanofibers with antibacterial property as potential wound dressings. *Int. J. Biol. Macromol.* **2014**, *68*, 92–97.
- (25) Pakdel, P. M.; Peighambaroust, S. J. Review on recent progress in chitosan-based hydrogels for wastewater treatment application. *Carbohydr. Polym.* **2018**, *201*, 264–279.
- (26) Wang, Y.; Zhao, W.; Qi, Z.; Zhang, L.; Zhang, Y.; Huang, H.; Peng, Y. Designing ZIF-8/hydroxylated MWCNT nanocomposites for phosphate adsorption from water: Capability and mechanism. *Chem. Eng. J.* **2020**, *394*, No. 124992.
- (27) Zhao, Y.; Yuan, P. Q.; Xu, X. R.; Yang, J. Y. Removal of p-nitrophenol by adsorption with 2-phenylimidazole modified ZIF-8. *Molecules* **2023**, *28*, 4195.
- (28) Venna, S. R.; Jasinski, J. B.; Carreon, M. A. Structural evolution of zeolitic imidazolate framework-8. *J. Am. Chem. Soc.* **2010**, *132*, 18030–18033.
- (29) Tsai, C. W.; Niemantsverdriet, J. W.; Langner, E. H. G. Enhanced CO<sub>2</sub> adsorption in nano-ZIF-8 modified by solvent assisted ligand exchange. *Microporous Mesoporous Mater.* **2018**, *262*, 98–105.
- (30) Amrhar, O.; El Gana, L.; Mobarak, M. Calculation of adsorption isotherms by statistical physics models: a review. *Environ. Chem. Lett.* **2021**, *19*, 4519–4547.
- (31) Li, J.; Chang, H.; Li, Y.; Li, Q.; Shen, K.; Yi, H.; Zhang, J. Synthesis and adsorption performance of La@ ZIF-8 composite metal-organic frameworks. *RSC Adv.* **2020**, *10*, 3380–3390.
- (32) Li, M.; Liu, Y.; Li, F.; Shen, C.; Kaneti, Y. V.; Yamauchi, Y.; Yuliarto, B.; Chen, B.; Wang, C. Defect-rich hierarchical porous UiO-66 (Zr) for tunable phosphate removal. *Environ. Sci. Technol.* **2021**, *55*, 13209–13218.
- (33) Xue, Y.; Xiang, P.; Jiang, Y.; Lian, H.; Mo, J.; Li, M. Influence of Ca<sup>2+</sup> on phosphate removal from water using a non-core-shell Fe<sub>3</sub>O<sub>4</sub>@ZIF-67 composites. *J. Environ. Chem. Eng.* **2020**, *8*, No. 104458.
- (34) Chen, Z.; Zhang, H.; Fan, G.; He, X.; He, Z.; Zhang, L. Diatomite composited with a zeolitic imidazolate framework for removing phosphate from water. *ACS Omega* **2022**, *7*, 26154–26164.
- (35) Gao, F.; Xu, X.; Yang, J. Removal of p-nitrophenol from simulated sewage using MgCo-3D hydrotalcite nanospheres: capability and mechanism. *RSC Adv.* **2022**, *12*, 27044–27054.
- (36) Loganathan, P.; Vigneswaran, S.; Kandasamy, J.; Bolan, N. S. Removal and recovery of phosphate from water using sorption. *Crit. Rev. Environ. Sci. Technol.* **2014**, *44*, 847–907.
- (37) Zhang, X.; Mai, Y.; Xian, X.; Hu, L.; Huang, J.; Yuan, H.; Lin, X. Adsorption and removal of phosphate from wastewater using lignin-based adsorbent modified with lanthanide: characterization, performance, and mechanisms. *Ind. Eng. Chem. Res.* **2022**, *61*, 18069–18079.
- (38) Liu, Y.; Sheng, X.; Dong, Y.; Ma, Y. Removal of high concentration phosphate by calcite: Effect of sulfate and Ph. *Desalination* **2012**, *289*, 66–71.
- (39) Li, R.; Wang, J. J.; Zhou, B.; Awasthi, M. K.; Ali, A.; Zhang, Z.; Gaston, L. A.; Lahori, A. H.; Mahar, A. Enhancing phosphate adsorption by Mg/Al layered double hydroxide functionalized biochar with different Mg/Al ratios. *Sci. Total Environ.* **2016**, *559*, 121–129.
- (40) Langmuir, I. The adsorption of gases on plane surfaces of glass, mica and platinum. *J. Am. Chem. Soc.* **1918**, *40*, 1361–1403.
- (41) Duranoğlu, D.; Trochimczuk, A. W.; Beker, U. Kinetics and thermodynamics of hexavalent chromium adsorption onto activated carbon derived from acrylonitrile-divinylbenzene copolymer. *Chem. Eng. J.* **2012**, *187*, 193–202.
- (42) Ho, Y. S.; McKay, G. Pseudo-second order model for sorption processes. *Process Biochem.* **1999**, *34*, 451–465.
- (43) Weber, W. J., Jr.; Morris, J. C. Kinetics of adsorption on carbon from solution. *J. Sanit. Eng. Div.* **1963**, *89*, 31–59.
- (44) Yoon, S. Y.; Lee, C. G.; Park, J. A.; Kim, J. H.; Kim, S. B.; Lee, S. H.; Choi, J. W. Kinetic, equilibrium and thermodynamic studies for phosphate adsorption to magnetic iron oxide nanoparticles. *Chem. Eng. J.* **2014**, *236*, 341–347.
- (45) Zeng, X.; Zhang, G.; Zhu, J. Selective adsorption of heavy metals from water by a hyper-branched magnetic composite material:

Characterization, performance, and mechanism. *J. Environ. Manage.* **2022**, *314*, No. 114979.

(46) Soliman, N. K.; Moustafa, A. F.; El-Mageed, H. R. A.; Abdel-Gawad, O. F.; Elkady, E. T.; Ahmed, S. A.; Mohamed, H. S. Experimentally and theoretically approaches for disperse red 60 dye adsorption on novel quaternary nanocomposites. *Sci. Rep.* **2021**, *11*, No. 10000.

(47) Dake, L. S.; Baer, D. R.; Friedrich, D. M. Auger parameter measurements of phosphorus compounds for characterization of phosphazenes. *J. Vac. Sci. Technol. A* **1989**, *7*, 1634–1638.

(48) Daou, T. J.; Begin-Colin, S.; Greneche, J. M.; Thomas, F.; Derory, A.; Bernhardt, P.; Legaré, P.; Pourroy, G. Phosphate adsorption properties of magnetite-based nanoparticles. *Chem. Mater.* **2007**, *19*, 4494–4505.

(49) Wang, J.; Xiang, L. Formation of ZnO rods with varying diameters from  $\epsilon$ -Zn(OH)<sub>2</sub>. *J. Cryst. Growth* **2014**, *401*, 279–284.

(50) Guan, T.; Li, X.; Fang, W.; Wu, D. Efficient removal of phosphate from acidified urine using UiO-66 metal-organic frameworks with varying functional groups. *Appl. Surf. Sci.* **2020**, *501*, No. 144074.

(51) Dai, Z.; Zhang, J.; Zhao, X.; Liu, X.; Zhang, J.; Liu, G. Synthesis of MgAl-LDH@ ZIF-8 composites by in situ growth method for highly efficient phosphate removal. *New J. Chem.* **2022**, *46*, 18295–18305.